ACS Catalysis

pubs.acs.org/acscatalysis

Research Article

Real-Time Noninvasive Analysis of Biocatalytic PET Degradation

Ronny Frank, Dana Krinke, Christian Sonnendecker, Wolfgang Zimmermann, and Heinz-Georg Jahnke*

Cite This: *ACS Catal.* 2022, 12, 25−35

Read Online

ACCESS | Metrics & More | Article Recommendations | Supporting Information

ABSTRACT: The Earth has entered the *Anthropocene*, which is branded by ubiquitous and devastating environmental pollution from plastics such as polyethylene terephthalate (PET). Ecofriendly and at the same time economical solutions for plastic recycling and reuse are being sought more urgently now than ever. With the possibility to recover its building blocks, the hydrolysis of PET waste by its selective biodegradation with polyester hydrolases is an appealing solution. We demonstrate how changing the dielectric properties of PET films can be used to evaluate the performance of polyester hydrolases. For this purpose, a PET film separates two reaction chambers in an impedimetric setup to quantify the film thickness- and surface area-dependent change in capacitance caused by the enzyme. The derived degradation rates determined for the polyester hydrolases PHL7 and LCC were similar to those obtained by gravimetric and vertical scanning interferometry measurements. Compared to optical methods, this technique is also insensitive to changes in the solution composition. AFM and FEM simulations further supported that impedance spectroscopy is a powerful tool for the detailed analysis of the enzymatic hydrolysis process of PET films. The developed monitoring system enabled both high-temporal resolution and parallel processing suitable for the analysis of the enzymatic degradability of polyester films and the properties of the biocatalysts.

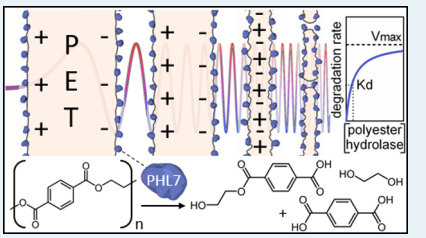

KEYWORDS: *electrochemical impedance spectroscopy, free-standing polymer film, polyester biodegradation, 3D printing, screening platform, PHL7, LCC*

1. INTRODUCTION

Polymer chemistry is one of the most advanced branches of material science and has produced synthetics that are indispensable in industry, medicine, and everyday life. These plastics often have physical, chemical, and physiological properties that are designed for optimal performance but often do not offer options for end-of-life recycling.[1,2] Thus, the transformation of polymer chemistry with respect to defossilization and the growth of a closed-loop economy represents a major challenge.

A part of the transformation can be achieved by tertiary recycling, thereby closing the loop from plastic synthesis to its degradation and resynthesis, especially if the starting materials of the polymers are recovered in an efficient and ecofriendly way.[3] One polymer where this approach is considered is PET, which accounts for 20% of the total plastic production worldwide that reached 359 million tons in 2018.[4,5] PET is widely used in the packaging and beverage industries and for the manufacture of textiles.[6]

Besides energy-intensive chemical hydrolysis,[7] glycolysis,[8] or pyrolysis,[9−12] the energy-efficient recycling of PET with enzymes has attracted considerable attention. Several polyester hydrolases, especially cutinase-like enzymes of bacterial or fungal origin, can attack synthetic polyesters such as PET or polycaprolactone (PCL)[2,13,14] due to a rather unspecific substrate recognition.[15] Thermostable PET hydrolases efficiently degrade PET with a high amorphous content but not crystalline or biaxial-oriented (BO) PET.[16] Products released by the enzymatic cleavage of PET are terephthalate (TPA), mono(2-hydroxyethyl terephthalate) (MHET), bis(2-hydroxyethyl terephthalate) (BHET), and ethylene glycol (EG).[14,17,18] The enzymatic polymer hydrolysis occurs more rapidly near the glass transition temperature of PET at around 70 °C; thus, the thermostability of the biocatalysts is beneficial.[19] Well-known polyester hydrolases that are able to attack PET are HiC,[19] TfCut1,[20] TfCut2,[21] and the leaf-branch compost cutinase LCC.[22] LCC (28 kDa) shows a 60% amino acid similarity to the lipase of *Thermomonospora curvata* and the cutinase of *Thermobifida fusca*.[23] It is also one of the most potent polyester hydrolases described previously and was only recently outperformed by the PHL7.[24] Typical for this class is the α/β hydrolase fold, the presence of the GXSXG box, and a conserved Ser−Asp−His triad, suggesting that these enzymes operate in a similar manner.[24]

The search for high-performance polyester hydrolases is tedious because few screening systems exist to quantify enzymatic PET-degrading activity.[25,26] In contrast, most analytical techniques such as NMR, HPLC, and calorimetry are used for a detailed investigation of the biochemical

Received: August 31, 2021
Revised: November 24, 2021
Published: December 9, 2021

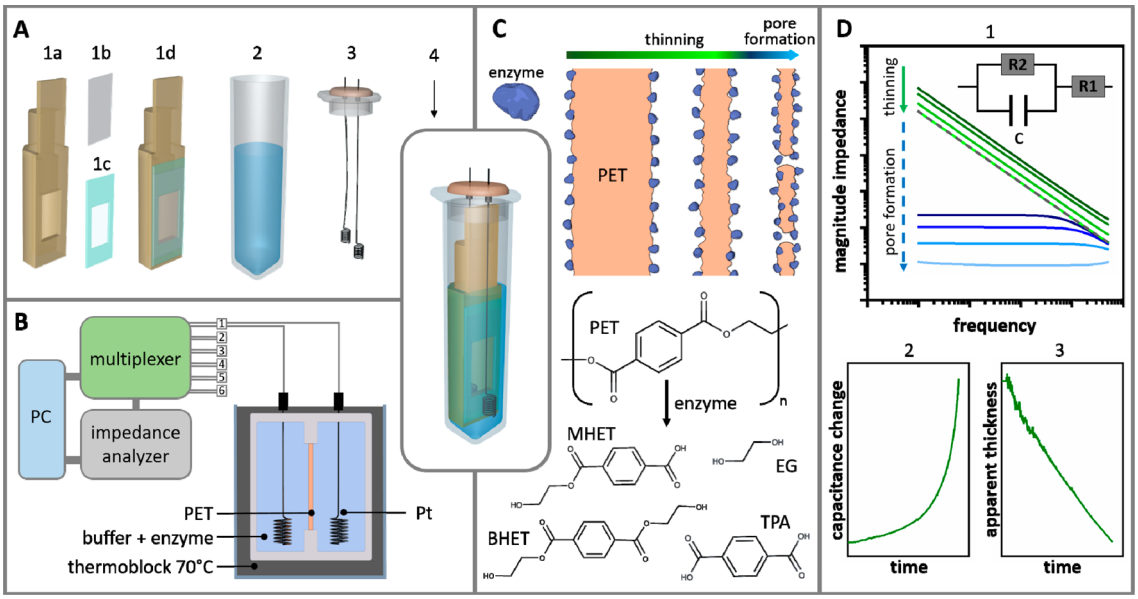

Figure 1. Impedance-based measurement setup for enzymatic G-PET film degradation analysis. (A) Assembly of a two-chamber reaction vessel. The 3D-printed polypropylene unit (1a) is combined with a PET film (1b) to define a reaction window with epoxy resin (1c) to form the finished insert (1d). Also shown are (2) the 2 mL reaction vessel, (3) the lid with platinum electrodes, and (4) the complete reaction unit. (B) Components of the impedance measurement system. (C) Illustration of the enzymatic degradation of a G-PET film, leading to the products mono(2-hydroxyethyl)-terephthalic acid (MHET), *bis*(2-hydroxyethyl)-terephthalic acid (BHET), terephthalic acid (TPA), and ethylene glycol (EG). (D) Impedance raw data derived from a degradation experiment (1) were analyzed by a Randles equivalent circuit model to give the change in capacitance (2) and in turn the apparent PET film thickness (3). Additional graphs can be found in Figure S6.

mechanism of these enzymes.[27] Typical applied methods to study the enzymatic hydrolysis of solid PET samples on a more general level include gravimetric analysis[20] and titrimetric methods such as the pH-stat.[28] Gravimetry has the advantage of not measuring a single product but instead the overall degradation of arbitrary PET material. A major drawback is that it operates discontinuously because the PET sample has to be removed from the enzyme solution and dried to be measured, leaving the analysis with a low temporal resolution. It is also labor-intensive because most steps are performed manually. In contrast, the pH-stat operates continuously by titrating the pH of the reaction solution that otherwise would shift during PET degradation due to the release of pH-active hydrolysis products such as TPA or MHET. However, the formation of pH-inactive products such as BHET or PET oligomers will not be monitored. Moreover, a mixture of products with different amounts of carboxyl groups will contribute unequally to the required amount of the titrant. This technique gives a sum signal of the overall hydrolysis and is suitable for the search of enzymes that degrade PET primarily to TPA. Due to the technical demands of the pH-stat system (pH electrode, stirrer, and injection system) and typical operating volumes in the double-digit milliliter range, miniaturization and parallelization are major challenges.

In this regard, optical methods such as spectrophotometry, fluorescence spectroscopy, and turbidimetry have been explored as screening tools. Using model substrates such as *p*-nitrophenol acyl esters (*p*NPA and *p*NPB), hydrolytic enzyme activity could be quantified photometrically by quantifying the released amount of *p*-nitrophenol.[29] The decrease of the absorbance of PET nanoparticles embedded into a hydrogel-matrix could be determined to assess the activity of polyester hydrolases in a turbidimetric setup in a 96-well format.[26] The use of model substrates and PET nanoparticles provides only limited information on the performance of the enzymes with plastic films or foils, which can show significant differences in degradability depending on their manufacturing process and thermal history. Another approach, specific for PET, uses the subsequent conversion of released TPA to fluorescent hydroxyl-phthalic acid (HOTH) by reactive oxygen species.[30−32] The conversion procedure requires the recurrent withdrawal of reaction solution aliquots, resulting in a similar temporal resolution as the weight loss approach. In sum, each method provides only a partial solution to the analysis of enzymatic PET degradation. A method combining the key points of applicability to different plastic materials, facile scalability, and a high temporal resolution, which is important for kinetic and stability studies of enzymes, has previously not been available.

Here, we developed a noninvasive and electronic tool to monitor the enzymatic degradation of PET films by real-time electrochemical impedance spectroscopy (EIS). This approach offers a straightforward way to reach a high degree of parallelization using established multiplexing techniques. This tool is also not prone to interference from additives, for example, those used in inhibition studies,[33] which can impair optical readouts. It uses actual PET films or foils as enzyme substrates without the need of model compounds[29] or the preparation of nanoparticles.[34,35] We show that EIS is suitable for assessing the kinetic data of the enzymatic polymer degradation, thereby showing potential as a screening method not only for PET but also for other thin polyester films such as polylactide (PLA) and PCL. High-speed impedance measurements allow the analysis of pore formation in plastic films during enzymatic degradation. To demonstrate the versatile aspects of the impedance-based degradation monitoring of PET samples, we used the polyester hydrolases PHL7 (PDB 7NEI) and LCC (PDB 4EB0), which have an equal molecular

https://doi.org/10.1021/acscatal.1c03963
ACS Catal. 2022, 12, 25−35

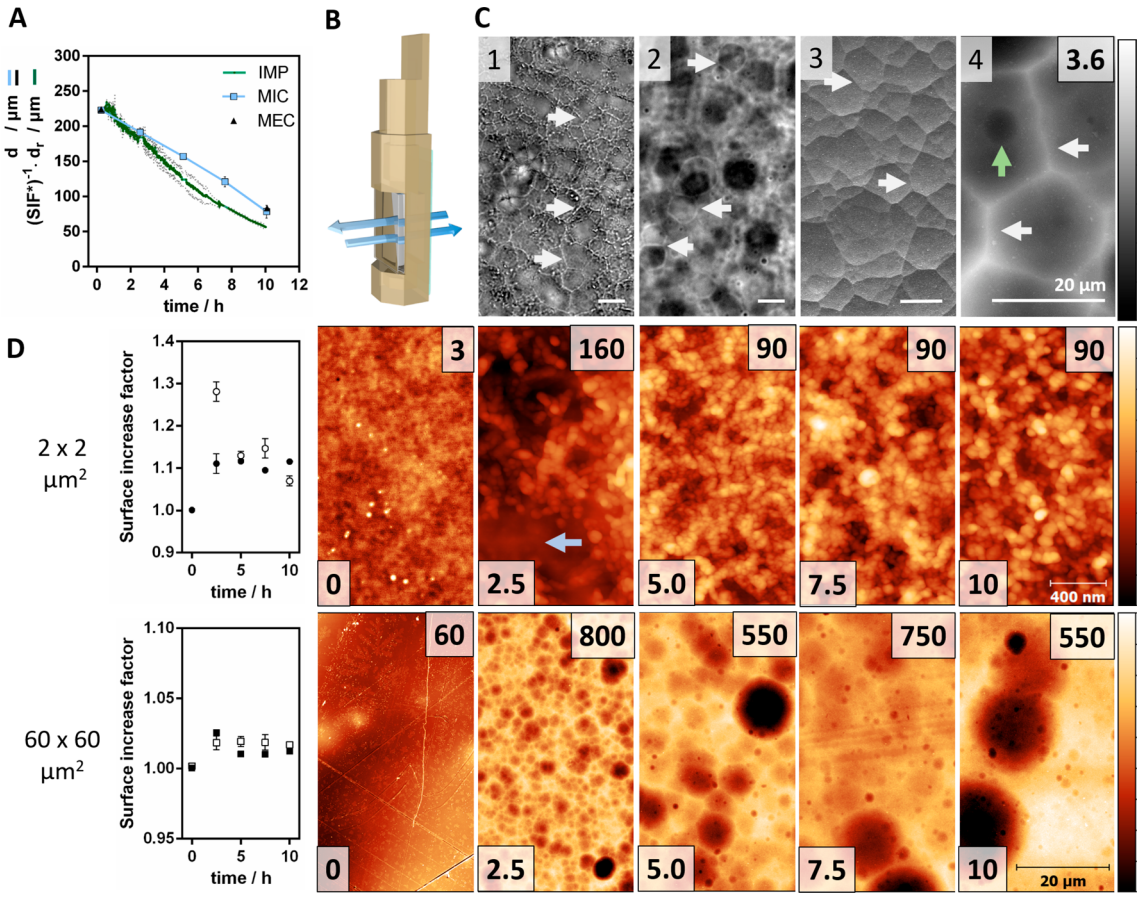

Figure 2. Microscopic analysis of the G-PET film thickness and surface roughness. (A) Thickness data measured impedimetrically (IMP), optically (MIC), and mechanically (MEC) at the same inserts (n = 2). (B) The 3D-printed polypropylene insert with a glass backside to allow light microscopic imaging. (C) Phase-contrast images of both the outside of the PET film (C1) and the inside (C2). SEM (C3) and AFM (C4) images of a PET surface showing crater-like structures after partial degradation by the polyester hydrolase PHL7. The height scale of the AFM image is given from 0 to 3.6 μm. White arrows mark crater edges used for focusing the outside and inside of the PET film. The green arrow marks a fresh degradation zone. (D) Time-dependent surface analysis of PET film degradation by PHL7 using AFM in the intermittent-contact mode. The linear height scale is given in nanometers from zero to the value in the upper-right corner of each image. Time is given in hours in the lower-left corner. The blue arrow marks area of low roughness. The surface increase factor was extracted from 2 × 2 μm^2 and 60 × 60 μm^2 512 × 512 px images for PHL7 (full symbol) and LCC (open symbol) (mean ± sd, $n \geq 2$), respectively. Experiments were conducted at 70 °C in 1 M potassium phosphate buffer (pH 7.8). Extended SIF data are provided in Table S1.

weight and a 55% sequence identity. We used amorphous PET films from Goodfellow (G-PET) with a crystallinity of 5−7%, which have been widely applied in enzymatic PET degradation studies.[4,36,24]

2. RESULTS AND DISCUSSION

2.1. Impedance Measurement Setup. The determination of the degradation of PET films was based on high-precision impedance spectroscopy. For this purpose, we developed a two-chamber reaction vessel (Figure 1A), which had a PET film as the thinnest material barrier between the two chambers that was filled with the electrolyte, and determined the impedance between the chambers. To the best of our knowledge this is the first report on such a setup. The few studies that used impedance spectroscopy to analyze degradation effects always used nonconductive polymers or coatings directly on an electrode material.[37] This is disadvantageous because delamination effects can compromise the validity of the impedimetric analysis.[38] With the setup of a free-standing polymer film, this issue is precluded. The first chamber was provided by means of a 3D-printed insert made of polypropylene, which was mounted with the PET film. The PET reaction window was defined on the inside by the geometry of the inset (Figure S1) and on the outside by an epoxy resin coating to prohibit enzymatic PET degradation outside the reaction window. The inserts were placed in a standard 2 mL reaction tube as the second chamber. A lid with two platinum electrodes formed a two-electrode setup for impedance spectroscopy, with one electrode on each side of the PET film. The platinum electrodes were chosen to be as large as possible to minimize self-impedance. The reaction vessel was placed in a standard thermoblock to achieve the optimal temperature required for the enzymatic reaction and to prevent external temperature changes that would influence the impedance measurements. In this sealed system, the impedance was recorded over a wide frequency range from 50 Hz to 5 MHz using a high-precision impedance analyzer and a multiplexer to observe multiple reaction units simultaneously (Figure 1B). PET degradation was observed over a period from several hours to days, while a single measurement could be performed within seconds. Thus, multiplexing was ideal for screening purposes because a high temporal resolution for 96 or more reaction units could be

https://doi.org/10.1021/acscatal.1c03963
ACS Catal. 2022, 12, 25−35

achieved with a single impedance analyzer. During the enzymatic degradation of the PET film, its thickness decreased (Figure 1C), which had a direct influence on the impedance signal. The PET film acted as a capacitive resistor, dominating the impedance signal until pores formed in the PET film that allowed an ion flow between the chambers (Figure 1D). From this point on, there was a multidecadal decrease in the magnitude of the impedance within seconds due to the size, length, and localization of the pores, which now determined the total impedance as an ohmic resistance. By determining the changes in impedance that were recorded from the starting time of the enzymatic reaction to just before the pore formation event, kinetics of the bulk PET film degradation could be derived. The raw impedance data were analyzed using the simplified Randles equivalent circuit model.[38−40] While the capacitance C and ohmic resistance R2 in parallel could be related to the PET film, there was an additional ohmic resistance R1 originating from the multiplexer, the contact wires, platinum wires, and the bulk electrolyte, which added up to 90 Ω when measured with a reaction vessel without a PET film (Figure S2). Thus, R1 was kept constant during the equivalent circuit modeling procedure.

Starting from ideal conditions to relate the capacitance C to the PET film, first we considered the capacitance $C_{t=0}$ according to eq 1, which is the sum of the capacitance of the PET film (C_{PET}) and the capacitance of the rest of the system (C_{rest}). The geometry of the PET film was a planar rectangle with an electrode on each of its sides. C_{PET} depends on the area (A) of the film, its relative permittivity (ε_r) and the film thickness (d) according to eq 2. Although the platinum electrodes themselves were not rectangular, the electrolyte of the reaction solution covered the PET film from both sides, acting similar to common electrolytic capacitors where this equation applies due to its conductivity.[41] A change in the PET film thickness (d) during an enzymatic degradation experiment caused a change in the measured capacitance (C), while there was almost no change in capacitance without enzyme, as could be seen in control experiments (Figure S3). Thus, C_{rest} could be assumed to be constant, leading to eq 3. By combining eq 3 with eq 1, we derived eq 4, which was free of C_{rest}. C_{rest} was determined to be about 10 pF (Figure S4). Solving eq 4 for the thickness expression resulted in eq 5, which represented the time-dependent apparent change of the PET film thickness. The initial thickness of the PET film ($d_{PET,t=0}$) was derived from a mechanical measurement at room temperature and corresponded to a capacitance of 4.6 pF for a 225 μm film thickness using the manufacturer's specification of the relative permittivity (ε_r = 3.0). Since the enzymatic degradation of the PET film was performed at 70 °C, a correction for the thermal expansion was considered, which for a thermal expansion coefficient of 2−8 × 10^{-5} K^{-1} according to the manufacturer's specification gave a maximal deviation of just +0.81 μm for the 225 μm film and thus could be neglected. In contrast, the temperature dependence of ε_r is far more important. The capacitance of the initial PET film at 70 °C as derived from approximation experiments using different sized reaction windows led to a value of 5.1 pF, which fits to a 225 μm film thickness assuming an ε_r of 3.3. This is in line with the extent of the temperature dependence of ε_r observed for PET[42] and correlated well with a FEM simulation (Figure S5). Thus, we calculated all apparent thickness values with ε_r =3.3 for the measurement frequency range. We referred to the film thickness as an apparent value because the deviation of the real-layer thickness from that measured according to eq 5 resulted from the fact that the area A fulfilled the ideal condition of being almost perfectly planar only at the beginning of the reaction. During degradation, the added roughness caused an increase in the surface area where more charge could be stored. Since the curvature of the nanostructures formed also plays a major role here,[43] an effective area A^* could be formulated, which is related to the real film thickness d_r according to eq 6. The effective area A^* is then a function of an effective surface increase factor SIF* (eq 7). For the G-PET film used here, a SIF of 1 at time t = 0 was confirmed by atomic force microscopy (AFM) imaging (Figure 2D), so SIF* should also be very close to 1. According to this, the determined values of the apparent film thickness correspond to the quotient of the real film thickness d_r and the effective surface increase factor SIF* (eq 9).

$$C_{t=0} = C_{PET,t=0} + C_{rest} \tag{1}$$

$$C_{PET,t=0} = \frac{\varepsilon_0 \varepsilon_r A}{d_{PET,t=0}} \tag{2}$$

$$C_{t=0} + \Delta C = \frac{\varepsilon_0 \varepsilon_r A}{d_{PET,t=0} + \Delta d_{PET}} + C_{rest} \tag{3}$$

$$C_{PET,t=0} + \Delta C = \frac{\varepsilon_0 \varepsilon_r A}{d_{PET,t=0} + \Delta d_{PET}} \tag{4}$$

$$d(t) = d_{PET,t=0} + \Delta d_{PET}(t) = \frac{\varepsilon_0 \varepsilon_r A}{C_{PET,t=0} + \Delta C(t)} \tag{5}$$

$$d_r(t) = \frac{\varepsilon_0 \varepsilon_r A^*(t)}{\frac{\varepsilon_0 \varepsilon_r A^*_{t=0}}{d_{PET,t=0}} + \Delta C(t)} \tag{6}$$

$$A^*(t) = A \cdot \mathrm{SIF}^*(t) \tag{7}$$

$$\mathrm{SIF}^*_{t=0} \approx 1 \tag{8}$$

$$\frac{d_r(t)}{\mathrm{SIF}^*(t)} = \frac{\varepsilon_0 \varepsilon_r A}{\frac{\varepsilon_0 \varepsilon_r A}{d_{PET,t=0}} + \Delta C(t)} \tag{9}$$

2.2. Correlation of PET Film Thickness Derived from Impedance and Optical Data. In the next step, we correlated the thickness data derived from impedance measurements to data that we extracted from phase contrast imaging as well as start- and end-point mechanical measurements (Figure 2). For this, we modified the design of the polypropylene insert to equip it with a glass plate of a 1 mm thickness on the backside to allow light microscopic analysis (Figure 2B). During the degradation of the PET sample with PHL7, craters were formed on both sides of the film. Adjacent craters formed edges ideal for optical focusing (Figure 2C) with a precision of ±1 μm. These structures were verified by scanning electron and atomic force microscopy. The thickness of the PET film was calculated as described by McLaren et al.[44] using a refractive index of 1.61 for the PET film (according to the manufacturer's specification) and an optical power P of zero given the macroscopic planar (not curved) character of the PET film. Figure 2A shows that the mechanical and optical measurements fit well together, while the impedance data showed a more pronounced decrease in the apparent film thickness over time, notably in the beginning of the reaction.

https://doi.org/10.1021/acscatal.1c03963
ACS Catal. 2022, 12, 25−35

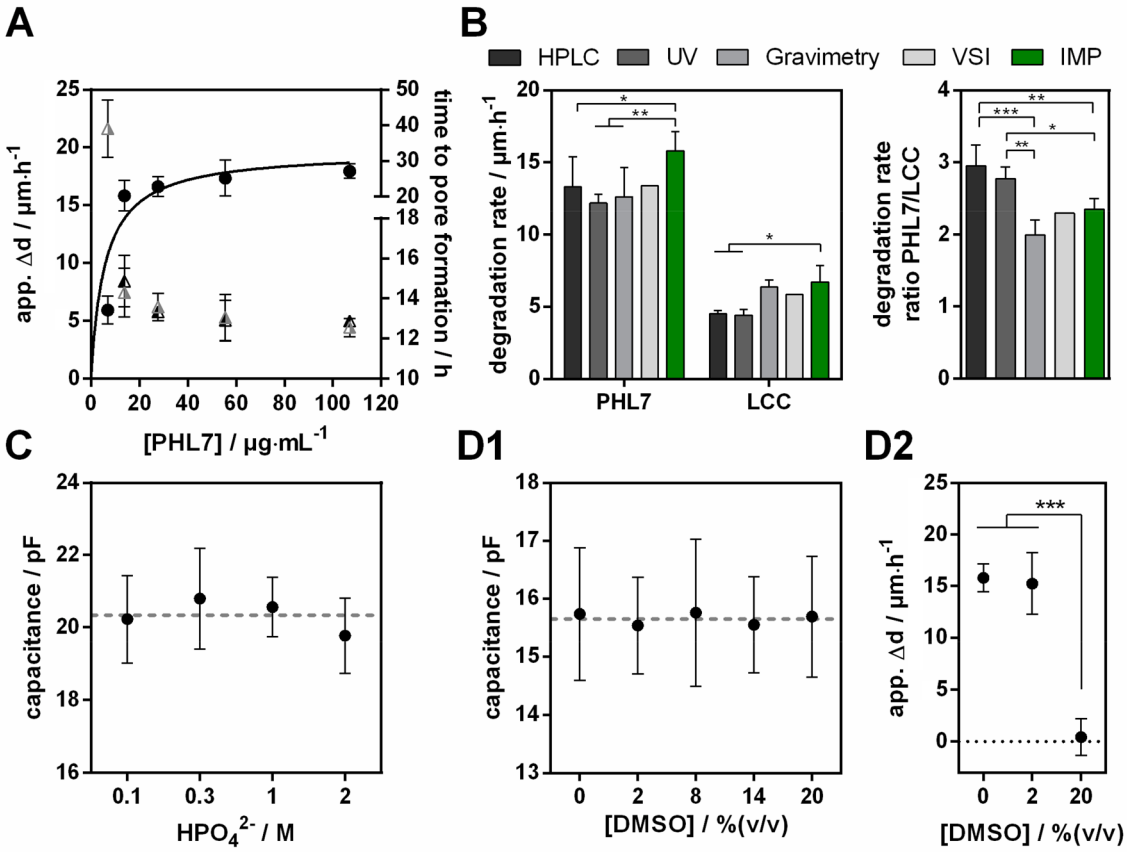

Figure 3. Impedimetrically determined enzymatic degradation of a G-PET film. (A) Saturation curve of PHL7 determined by a capacitance assessment (circle, left *y*-axis) and the time to pore formation (triangle, right *y*-axis) of the 225 μm PET film (78 mm^2). Black half triangles show measured values, and gray half triangles show the calculated time based on the constant capacitance-derived degradation rate. For the lowest enzyme concentration (6.95 μg·mL^{-1}), no pore formation was observed. (B) Comparison of the degradation rates obtained with 13.9 μg·mL^{-1} PHL7 and LCC for the dissolution of G-PET. UV indicates the UV absorbance measurement, VSI indicates the vertical scanning interferometry, and IMP indicates impedance spectroscopy (mean ± sd, n = 3 (HPLC and UV), 6 (gravimetry), 8 (IMP), or 1 (VSI)). (C) Influence of the hydrogen phosphate buffer concentration on the base capacitance. (D) Influence of the DMSO content on the base capacitance (1) and activity of PHL7 in the presence of different amounts of DMSO (mean ± sd, $n \geq 3$) (2). Experiments were conducted at 70 °C in 1 M potassium phosphate buffer (pH 7.8).

The mechanical and the optical measurements probably slightly overestimated the mean thickness of the PET film due to the edges of the craters, which were in contact or in focus during the measurement and thus did not include the mean decrease in thickness according to the depth of the craters. We estimated this effect to contribute possibly up to 3 μm for each side of the PET film, resulting in a total of 6 μm deviation based on the AFM data. However, this effect was obviously insufficient for explaining the difference of up to 30 μm we observed in the impedance data. We consider the change in the surface area and thus a surface increase factor bigger than 1 as a main factor of the observed deviation. In this case, the surface area increased with increasing roughness, enabling more charge to be stored. The inverse relation between the capacitance and the film thickness would then lead to an apparent stronger decrease in film thickness. We measured the increase in surface area by AFM (Figure 2D) for image sections of 2 × 2 and 60 × 60 μm^2. Within the first hours, we observed the largest change of the surface increase factor, starting from almost perfect planarity with 1.00 ± 0.00 (60 μm, 0 h) and 1.00 ± 0.00 (2 μm, 0 h) and reaching 1.03 ± 0.00 (60 μm, 2.5 h) and 1.11 ± 0.01 (2 μm, 2.5 h), respectively, within 2.5 h. After 5 h, the nanoscopic features (2 × 2 μm^2 images) stayed almost constant at a surface increase factor of 1.10, maintaining a kind of steady-state morphology. The microscopic increase factor (60 × 60 μm^2) diminished slightly to 1.01. Similar results were obtained with the polyester hydrolase LCC (Figures 2D and 7). Thus, the nanoscopic roughness attributed far more to the overall surface area increase than the microscopic one. To investigate the influence of the surface roughness on the capacitance and thus the apparent film thickness, we performed FEM simulations with different surface increase factors (Figure S8). An increase in area of just 5% led to a capacitance increase by a factor of 1.28, an increase in area of just 10% led to a capacitance increase by a factor of 1.38, and an increase in area of 15% led to a capacitance increase by a factor of 1.44. Thus, the observed surface increase in the range of 10% was sufficient to explain the difference between the optically and mechanically determined film thickness of 80 μm after 10 h, which is equivalent to a film capacitance of 15 pF, and the calculated apparent film thickness of 55 μm based on impedimetric monitoring (equivalent to 20 pF, a factor of 1.33). The impedimetrically monitored degradation therefore mapped the changes in both the film thickness and the surface topology. This allowed the detection of degradation processes that might

https://doi.org/10.1021/acscatal.1c03963
ACS Catal. 2022, 12, 25−35

be missed by means of optical or mechanical measurements but it also created the difficulty of differentiating between both effects. With respect to the aim of taking the surface topology into account, high-resolution imaging showed that the surface enlargement, for both PHL7 and LCC, hardly changed between 5 and 10 h of reaction. Therefore, during this steady-state period the influence of surface enlargement should be comparable, enabling an estimation of the degradation rate. Quantitatively, this is considered in detail in section 2.3. We anticipate that by using impedance measurements it would be possible to detect PET-degrading activity in a wide range of polyester hydrolases due to the similarity of their catalytic mechanisms.[45,46]

From a morphological point of view, craters were formed on the microscopic scale that grew with time, while new craters continuously formed at every stage. The nanoscopic features showed randomly distributed grains of a similar size after degradation times from 2.5 to 10 h. However, notably after 2.5 h we observed local areas with a lower roughness and a finer graining compared to those in later stages, which occurred particularly in valley regions (see also Figure S9). The finer graining was primarily visible in phase images. We hypothesize that these represent highly disordered amorphous areas, which could be degraded slightly faster than the coarse-grained areas. After 5 h of degradation, only a few of these amorphous areas, which were spatially very limited, could be observed, and after a degradation time of 7.5 h they disappeared. We assume that this observed heterogeneity is caused by the thermal treatment in the manufacturing process. In this regard, impedance spectroscopy offers a new approach to study enzymatic PET degradation because it inherently records the surface roughness and moreover its ability to have a high temporal resolution. This allows us to fingerprint different types of PET films, which differ in their amorphous and crystalline heterogeneity and thus degradability. When we degraded mechanically recycled PET (R-PET) from a postconsumer PET thermoform clamshell packing (crystallinity 4.5%),[24] a considerable different time profile was found compared with that of the more homogeneous virgin G-PET film of a similar crystallinity (5−7%), which was indicated by zones of faster and slower degradation rates (Figure S10).

2.3. Enzymatic PET Degradation Kinetics. Figure 3A shows the apparent rate of G-PET film degradation as a function of the enzyme concentration of the highly active polyester hydrolase PHL7. We observed a typical saturation curve with a V_{max} of 19.7 $\mu m \cdot h^{-1}$ according to a one-site specific binding nonlinear regression. This was the simplest model to fit the data with the assumption that the enzyme molecules occupy a finite amount of binding sites on the PET. In addition to the analysis of the capacitive change, which enables a real-time quantification of the degradation, recording of the formation of pores in the film furthermore allowed an independent qualitative rate estimation of the enzymatic degradation. Here, the multidecadal jump was recorded, which provided information about at what time the film locally became so thin that ion passage could take place, similar to a yes or no decision. Since this is also a stochastic process that can occur at different times depending on possible defects in the film, it can only be used as a benchmark for an enzyme evaluation when a sufficiently large number of replicates are available. However, for PET with a high homogeneous film thickness and only small or no defects, pore-forming events between replicates can also temporally occur quite close to one another, deviating by only 1 min after a 13 h reaction time (Figure S11). Based on the calculated degradation rate from the capacitance data in the 5−10 h reaction window, the time of pore formation could also be estimated accurately (Figure 3A).

To investigate the suitability of the impedance spectroscopy method for evaluating PET-degrading enzyme performance, we determined the degradation rates and ratios of the two polyester hydrolases PHL7 and LCC at a a concentration of 13.9 $\mu g \cdot mL^{-1}$, which is equivalent to 500 nM (Figure 3B).[22,23] We compared the impedimetrically derived data with degradation rate determinations made with HPLC, UV, gravimetric, and vertical scanning interferometry (VSI) measurements. The impedance-derived degradation rate for PHL7 (15.8 ± 1.3 $\mu m \cdot h^{-1}$) was around 20% higher compared with the determinations made by HPLC (13.3 ± 2.1 $\mu m \cdot h^{-1}$), UV (12.2 ± 0.6 $\mu m \cdot h^{-1}$), gravimetry (12.6 ± 2.0 $\mu m \cdot h^{-1}$), and VSI (13.4 $\mu m \cdot h^{-1}$). In case of the LCC, the impedance data resulted in a degradation rate of 6.7 ± 1.1 $\mu m \cdot h^{-1}$, thus being very close to the gravimetric (6.4 ± 0.5) result and around 15% higher than the VSI-derived data (5.8 $\mu m \cdot h^{-1}$). The HPLC (4.5 ± 0.3 $\mu m \cdot h^{-1}$) and UV data (4.4 ± 0.4 $\mu m \cdot h^{-1}$) differed more pronouncedly from the other three methods. In terms of the comparison of PHL7 and LCC, the highest ratios were found for the HPLC (3.0 ± 0.3) and UV (2.8 ± 0.2) methods, while the gravimetric method showed the lowest one (2.0 ± 0.2). Ratios derived from VSI (2.3) and impedance (2.3 ± 0.2) methods lay in between. The results showed that the impedance measurements overestimated the degradation rates compared to the other methods, likely due to the influence of the film surface roughness as stated earlier. On the other hand, it also showed that there was no significant difference in the ratio of the degradation rates of the enzymes compared to the weight loss and VSI methods. Major differences were observed between the methods that used the reaction solution as the basis of the analysis (HPLC and UV) compared with those that use the PET sample (VSI, gravimetric, and impedimetric methods). In view of a screening application for enzyme optimization, the observed method-to-method variations are not critical, since screenings are generally based on relative comparisons, e.g., with a reference enzyme, with the aim of identifying candidates with a multiple of the reference activity (hits).[47] For identified hits, detailed investigations using more elaborate methods would follow.

In a further step to characterize the impedance spectroscopy method, we also tested the influence of the electrolyte concentration on the overall capacitance. For a range from 0.1 to 2 M hydrogen phosphate buffer, we found no significant change of the base capacitance (Figure 3C). This is in line with a FEM simulation of thick (225 μm) and thin (12 μm) PET films, where the conductivity of the buffer showed no effect on the impedance spectra (Figure S12). Therefore, the electrolyte concentration could be changed during an experiment without influencing the impedance measurement. This is also crucial since the degradation of PET produces terephthalic acid, thus altering the electrolyte concentration during a reaction. As the impedance measurement only requires a conductive medium to derive well-defined spectra, any other electrolyte should also be well suited. We also investigated the effect of different amounts of DMSO, up to 20% (v/v), on the base capacitance and the enzyme activity. We chose DMSO as a test solvent due to its dissolution qualities to EG and BHET in the chemical glycolysis of PET,[48] its good miscibility with water, and its low

https://doi.org/10.1021/acscatal.1c03963
ACS Catal. 2022, 12, 25−35

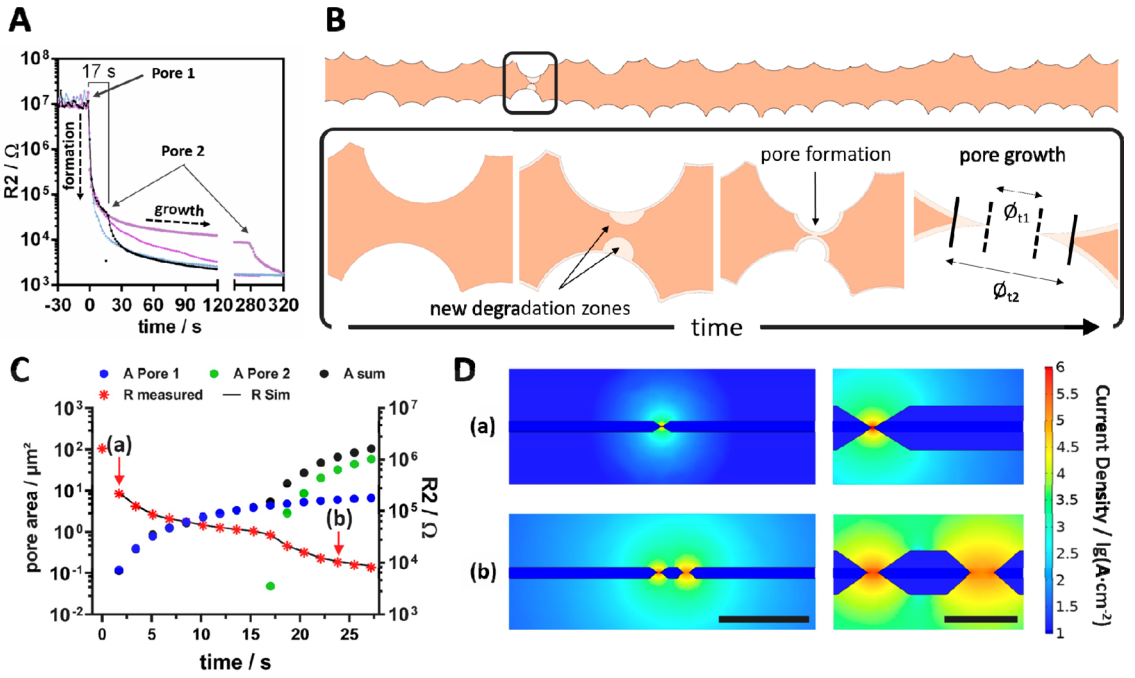

Figure 4. Analysis of pore formation in the G-PET film by high-speed impedance spectroscopy. (A) Ohmic pore resistance as a function of time. The second strong decrease in R2 occurred in one of the test samples 17 s after the first pore formation, probably indicating the formation of a second pore. (B) Model of the pore formation process. (C) FEM Simulation of the pore formation for the black graph in panel A, with a second pore occurring after 17 s. The R2 values derived from the simulated pore area were adjusted to the values for R2 derived from measurements. (D) FEM-simulated current density plots for a double-cone-shaped pore geometry for time point (a) and (b) as marked in C. The scale bar is 50 μm in the left images and 10 μm in right images. More plots can be found in the SI (Figure S13).

volatility. In the control experiment we observed no significant change in the base capacitance even when 20% DMSO was present (Figure 3D1). This is especially beneficial for screenings with additives as it demonstrates that the measurement is not susceptible to a certain degree of nonconducting compounds. Adding DMSO to 2% did also not alter the degradation rate of PHL7 but inactivated the enzyme at a content of 20% (Figure 3D2). This was also confirmed visually as no dissolution of the PET film was observed. PHL7 inactivation is in accordance with the typical loss in function of enzymes at high organic solvent concentrations.[49]

2.4. Analysis of Pore Formation in G-PET Films Degraded with PHL7 by High-Speed Impedance Spectroscopy. During pore formation when the PET film becomes permeable for ions, the ohmic resistor R2 drops by multiple decades, thus completely altering the impedance signal. To measure this event in more detail, a high temporal resolution is required. The lower the excitation frequency, the earlier the pore formation event can be detected, since in this case the ions have more time to create a measurable ion flow even through very small permeation sites. However, low frequencies are accompanied by a longer runtime of the measurement to guarantee sufficient precision. Using a high-precision impedance analyzer optimized for measurement speed especially in the low frequency range, we were able to record impedance spectra of up to six parallel reactions every 1.7 s using a steady multiplexing loop without idle time of the impedance analyzer (Figure 4A). At the breakthrough of the film, the resistance of most of the reaction samples dropped from above 10 MΩ to values between 1 and 10 KΩ within 1 min before slowly decreasing steadily. In the following minutes, a stronger stepwise decrease in resistance was observed in some cases, probably due to the formation of further pores. We assume that the pore formation started in the crater regions of the film caused by the enzyme when two distinct craters on either side of the PET film happened to be opposite to each other (Figure 4B). When new degradation zones appeared inside the crater, as can be seen in Figure 2C4, a pore could easily form. Due to the crater geometry, the pore would enlarge rapidly due to PET degradation that could now occur not only out-of-plane but also in-plane. To investigate this pore formation process in more detail, we created a FEM model based on a double cone-shaped pore geometry (Figure 4C). Assuming a residual film thickness of 12 μm based on the determined capacitance directly before the first pore formation, we reconstructed the ohmic pore resistance of a high-speed data set (black graph in Figure 4A) to derive the corresponding change in the pore area (Figure S13). Furthermore, the occurrence of a second pore after 17 s was included in the FEM simulation. This model was able to describe the changes in the impedance spectra in a straightforward manner. The combination of impedance spectroscopy and the FEM simulation thus allows insight into the enzymatic degradation of PET not only up to the point of pore formation but also beyond. In perspective, being able to monitor the formation and growth of pores in the PET film with a high temporal resolution using impedance spectroscopy offers in principle another way to determine enzymatic degradation rates. To accurately perform this analysis, a defined pore would have to be introduced into the PET film, for example, by a UV-based femtosecond laser ablation. Due to the high sensitivity of the impedance signal to ion fluxes, this approach could offer an analysis time tremendously decreased from hours or days to minutes. Moreover, due to the minuscule dimension of the required pore, this could be combined with a miniaturization of the

https://doi.org/10.1021/acscatal.1c03963
ACS Catal. 2022, 12, 25−35

polymer film window, resulting in a substantial increase in the sample density.

In conclusion, impedance spectroscopy was shown to be a versatile approach for studying the enzymatic degradation of polymer films in terms of surface and thickness changes as well as pore formation and growth that has not been exploited so far. While it should be kept in mind that surface roughness can lead to some overestimation of absolute degradation rates relative to the layer thickness determination, this method proved to be a useful tool for assessing enzyme activity comparable to gravimetric and VSI methods. Since the method is robust against changes in the electrolyte concentration as well as contaminants and also works in the presence of nonconducting solvents, it also offers an alternative to optical methods. Analyses can be performed in a highly parallelized manner by multiplexing and with a lower setup effort, for example, by using planar electrode structures in a sandwich design. Furthermore, as an electronic measuring method, the automation of data processing is possible. In sum, impedance spectroscopy carries the potential to be a compelling novel tool for the analysis of polyester hydrolases and the degradability of polyester films.

3. EXPERIMENTAL SECTION

Expression and Purification of the Polyester Hydrolases PHL7 and LCC. A detailed method is described elsewhere.[24] In short, PHL7 and LCC were recombinantly expressed as mature fusion proteins with a C-terminal His tag in *Escherichia coli* BL21(DE3) using the pET26b(+) vector system. The intracellular fraction was purified by IMAC chromatography. The eluate obtained was treated for 30 min at 60 °C, followed by size-exclusion chromatography, to obtain highly purified enzyme preparations.

Manufacturing of PP/PET Inserts. Polypropylene (PP) inserts were 3D printed one by one using an Ultimaker 3 Extended (Ultimaker BV, Netherlands) system and a transparent polypropylene filament (Ultimaker BV, Netherlands) at a layer resolution of 100 μm (printing PP-inserts in parallel was not suitable due to small defects that probably occurred because of the movement of the print head between single units). The PP surface surrounding the reaction window was roughened with emery paper. PP inserts were washed with 70% ethanol and ultrapure water and dried at room temperature. Amorphous PET film (G-PET, thickness of 225 μm ± 1 μm) was purchased from Goodfellow GmbH (Bad Nauheim, Germany), and postconsumer PET thermoform clamshell packing (Guillin, Ornans, France) was obtained from a local supermarket. The PET films were cut into pieces to a size that jutted out of the reaction window by 2 mm to each side. PET pieces were bonded to the PP insert using epoxy resin (EPOTEK 302−3M), and the samples fixed with two clips during curing. To generate a defined PET window on the outer surface, the protruding PET film was sealed with epoxy resin, thus giving a combined PET surface area of the front and back side of 78 mm^2.

Impedimetric Monitoring of PP/PET Inserts. PP/PET inserts were cleaned for 10 min in 0.5% SDS on a shaker, washed with ultrapure water, rinsed with 70% ethanol, and dried. Inserts were filled with 300 μL of the reaction buffer (1 M potassium hydrogen phosphate buffer, pH 7.8, and 13.9 μg·mL^{-1} (500 nM) PHL7 or LCC, unless stated otherwise) and placed in a 2 mL reaction tube containing 600 μL of reaction buffer. This unit was transferred into a thermomixer (Eppendorf, Germany) closed with the electrode lid, so that one platinum electrode was placed on the inside and the other one on the outside of the PP/PET insert. The temperature of the thermomixer was set to 70 °C. Platinum electrodes were connected to an in-house multiplexer controlled by self-developed software (IMATadvanced v2021)[50] written in LabView (National Instruments). Impedance was measured from 50 Hz to 5 MHz (61 frequency points) with a signal amplitude of 100 mV every minute with up to six samples in parallel using an Agilent 4294A high-precision impedance analyzer (Agilent Technologies). For high-speed measurements, impedance was measured from 500 Hz to 1 MHz (35 frequency points) in a uniformly circulating multiplexing of six parallel samples using a Sciospec ISX-3v2 high-precision impedance analyzer (Sciospec GmbH) with an optimized acquisition speed in the lower frequency range, thus resulting in a cycle acquisition rate of 1.3 to 1.7 s corresponding to around 250 ms per single spectrum.

Analysis of Impedance Data. Raw data were analyzed using the simplified Randles equivalent circuit model consisting of an ohmic resistor (R1) in series with the parallel combination of a capacitance (C) and a second ohmic resistor (R2). The fitting procedure was performed using a MATLAB script with the Nelder−Mead method as described elsewhere.[51] The resistance R1 corresponded to the PET-free cell resistance of the system and was derived from an impedance measurement of a PP insert with an open reaction window that was done using an equivalent circuit model consisting of a capacitance (C_{dl}) in series to R1. The determined R1 value (90 Ω) was used as a constant for the raw data fitting when a PET film was present so that only C and R2 were allowed to change. Capacitance was correlated to the PET thickness by assuming every change in C was caused by the thinning of the PET film (Figure S5). To calculate the degradation rate of PET in micrometers per hour, the apparent thickness change between 5 and 10 h of reaction time was used and fitted with a linear regression. The correlation coefficient of the regression had to fulfill a value of >0.99, otherwise the time region was shortened to compensate for nonlinearity.

Degradation Analysis by Nonimpedance Measurements. The impedimetric and all comparative analyses were performed with PHL7 and LCC batches that were prepared identically. An equal enzyme concentration (13.9 μg·mL^{-1}, equal to 500 nM) and a standard PET sample (G-PET) were used for all analyses. Weight loss measurements were performed as previously described.[24] The UV spectroscopic determination of aromatic hydrolysis products in reaction supernatants was determined at 240 nm with a Synergy MX micro plate reader (BioTek Instruments Inc., Winooski, VT). Samples were diluted with 1 M potassium phosphate buffer (pH 7.8), and 100 μL aliquots were measured in microplates (UV-STAR 655801, Greiner Bio-One, Kremsmünster, Austria). An equimolar mixture of TPA and MHET was used for calibration in the linear range between 5 to 750 μM (TPA equivalents, TPA_{eq}). The UV-derived release rate of TPA_{eq} between the reaction time of 5−10 h was translated into milligrams of PET per hour using a molar mass of 166 g·mol^{-1} for TPA and that of 192 g·mol^{-1} for the PET monomer. From this the total amount of PET was calculated and translated into a decrease in micrometers per hour using a starting mass of 45 mg and a PET thickness of 225 μm. Similarly, degradation rates in micrometers per hour were calculated from the HPLC

https://doi.org/10.1021/acscatal.1c03963
ACS Catal. 2022, 12, 25−35

data from Sonnendecker et al.[24] VSI data were taken from Sonnendecker et al.[24]

Surface Analysis by Atomic Force Microscopy. AFM samples were prepared as followed. A piece of the G-PET film of the same size as that used for the PP inserts was bonded to a 1 mm thick glass slide that fit into a 2 mL standard reaction vessel. The degradation reaction was performed as described above. Subsequently, the PET film was washed in a 1% sodium dodecyl sulfate solution, rinsed with ultrapure water, and dried in a nitrogen stream. The PET surface was analyzed using a JPK Nanowizard III (Bruker Nano GmbH) system with a TESP-HAR cantilever (Bruker Nano GmbH) in the intermittent contact mode in air with 512 × 512 measurement points. AFM images were processed using Gwyddion 2.47. First, the mean plane was subtracted from the height data, and rows were aligned using the internal median of differences method. The surface area was extracted by the statistical quantities tool based on triangulation and related to the projected area to give the surface increase factor.

Finite Element Model (FEM) Simulation. The FEM simulation was done as a 3D model using the electrical current (ec) physics from the AC/DC-module of COMSOL Multiphysics 5.3 (Comsol Multiphysics GmbH) and a frequency domain study. Geometry data for the PET films were taken from Figure S1 (4.3 × 9.1 mm^2) with buffer domains on both sides (relative permittivity of 80, electrical conductivity of 11 $S \cdot m^{-1}$ measured with 1 M potassium hydrogen phosphate buffer and platinum electrode domains). To recapitulate the electrode−electrolyte double layer, a capacitance of 0.34 $F \cdot m^{-2}$ was determined from system impedance data (Figure S2). Additionally, the residual capacity of the whole measurement system, including the measurement chamber (see Figure S4), was determined for each analyzed and simulated experiment, with values in the range of 8−11 pF. This was included in the FEM model as a parallel circuit by the use of a coupled electrical circuit (cir) physics. To simulate the impedance measurement, an alternating electrical field with a 100 mV amplitude at the measurement electrode and a ground connection at the counter electrode was applied. The simulation was done using a fully coupled direct solver with the mesh size normal for the buffer and electrode domains, a mesh refinement step (factor 1) for the PET film domain, and a further mesh refinement step (factor 2) for the pore domain.

Optical and Mechanical Determination of PET Film Thickness. The microscopic determination of the PET film thickness was performed using PP inserts with an additional glass window on the backside to allow transmitted light images in a phase-contrast microscope (Eclipse TE2000-U, Nikon instruments Europe, BV, Netherlands) with a 20× objective lens. Inserts were placed on a microscope slide with a drop of 0.2 M potassium hydrogen phosphate buffer, pH 7.8. The top and bottom sides of the PET film were focused, and the path difference was recorded using the adjustment wheel with a micrometer scaling. The thickness was calculated according to McLaren et al.[44] using a refractive index of 1.61 for PET. The mechanical determination was performed using a digital micrometer (QuantuMike IP65, Mitutoyo).

Statistics. Graphpad Prism 5 (GraphPad Software, Inc.) was used for all statistical analysis. Presented graphs are given as the mean ± sd unless stated otherwise. The significance of the mean difference was analyzed by one-way ANOVA and Tukey posthoc tests, considering $*P < 0.05$ as significant, $**P < 0.01$ as very significant, and $***P < 0.001$ as extremely significant. One-site specific binding nonlinear regression was performed with the implemented prism function using the model $Y = B_{max} \times X/(K_d + X)$.

■ ASSOCIATED CONTENT

Supporting Information

The Supporting Information is available free of charge at https://pubs.acs.org/doi/10.1021/acscatal.1c03963.

Geometry details of the polypropylene (PP) insert, impedance data of a fully open PP insert, capacitance data, FEM simulations, AFM images, degradation profile of R-PET, deviation of the time of the pore formation event, and influence of the solvent content on the capacitance analyzed by FEM simulation (PDF)

■ AUTHOR INFORMATION

Corresponding Author

Heinz-Georg Jahnke − *Centre for Biotechnology and Biomedicine, Molecular Biological-Biochemical Processing Technology, Leipzig University, D-04103 Leipzig, Germany;* orcid.org/0000-0001-6615-7092; Email: heinz-georg.jahnke@bbz.uni-leipzig.de

Authors

Ronny Frank − *Centre for Biotechnology and Biomedicine, Molecular Biological-Biochemical Processing Technology, Leipzig University, D-04103 Leipzig, Germany;* orcid.org/0000-0001-5455-8497

Dana Krinke − *Centre for Biotechnology and Biomedicine, Molecular Biological-Biochemical Processing Technology, Leipzig University, D-04103 Leipzig, Germany*

Christian Sonnendecker − *Institute of Analytical Chemistry, Leipzig University, D-04103 Leipzig, Germany*

Wolfgang Zimmermann − *Institute of Analytical Chemistry, Leipzig University, D-04103 Leipzig, Germany*

Complete contact information is available at: https://pubs.acs.org/10.1021/acscatal.1c03963

Notes

The authors declare no competing financial interest.

■ ACKNOWLEDGMENTS

This work was funded by the Federal Ministry for Economic Affairs and Energy based on a resolution of the German Bundestag (BMWi, STARK program Grant 46SKD023X) and the European Union (EFRE) and is cofinanced from tax revenues on the basis of the budget passed by the Saxon state parliament (SMWK) (project Akto-TronikSen Grant 100376525 and Grant 100549990). The authors further acknowledge funding from the European Union's Horizon 2020 research and innovation program under grant agreement no. 887913 (ENZYCLE), and from the Saxon State Ministry for Science, Culture, and Tourism (SMWK) (Project no. 100387903) in the framework of the ERA CoBioTech project MIPLACE.

■ REFERENCES

(1) Ellis, L. D.; Rorrer, N. A.; Sullivan, K. P.; Otto, M.; McGeehan, J. E.; Roman-Leshkov, Y.; Wierckx, N.; Beckham, G. T. Chemical and biological catalysis for plastics recycling and upcycling. *Nature Catalysis* **2021**, *4*, 539−556.

(2) DelRe, C.; Jiang, Y.; Kang, P.; Kwon, J.; Hall, A.; Jayapurna, I.; Ruan, Z.; Ma, L.; Zolkin, K.; Li, T.; Scown, C. D.; Ritchie, R. O.; Russell, T. P.; Xu, T. Near-complete depolymerization of polyesters with nano-dispersed enzymes. *Nature* **2021**, *592*, 558−563.
(3) Lee, A.; Liew, M. S. Tertiary recycling of plastics waste: an analysis of feedstock, chemical and biological degradation methods. *J. Mater. Cycles Waste Manage.* **2021**, *23*, 32−43.
(4) Tournier, V.; Topham, C. M.; Gilles, A.; David, B.; Folgoas, C.; Moya-Leclair, E.; Kamionka, E.; Desrousseaux, M. L.; Texier, H.; Gavalda, S.; Cot, M.; Guemard, E.; Dalibey, M.; Nomme, J.; Cioci, G.; Barbe, S.; Chateau, M.; Andre, I.; Duquesne, S.; Marty, A. An engineered PET depolymerase to break down and recycle plastic bottles. *Nature* **2020**, *580*, 216−219.
(5) PlasticsEurope. Plastics − the Facts 2019. https://plasticseurope.org/de/wp-content/uploads/sites/3/2021/10/Plastics_the_facts_2019.pdf (accessed 2021-11-24).
(6) Kawai, F. The Current State of Research on PET Hydrolyzing Enzymes Available for Biorecycling. *Catalysts* **2021**, *11*, 206.
(7) Yoshioka, T.; Motoki, T.; Okuwaki, A. Kinetics of Hydrolysis of Poly(ethylene terephthalate) Powder in Sulfuric Acid by a Modified Shrinking-Core Model. *Ind. Eng. Chem. Res.* **2001**, *40*, 75−79.
(8) Genta, M.; Iwaya, T.; Sasaki, M.; Goto, M.; Hirose, T. Depolymerization Mechanism of Poly(ethylene terephthalate) in Supercritical Methanol. *Ind. Eng. Chem. Res.* **2005**, *44*, 3894−3900.
(9) Kenny, S. T.; Runic, J. N.; Kaminsky, W.; Woods, T.; Babu, R. P.; Keely, C. M.; Blau, W.; O'Connor, K. E. Up-cycling of PET (polyethylene terephthalate) to the biodegradable plastic PHA (polyhydroxyalkanoate). *Environ. Sci. Technol.* **2008**, *42*, 7696−7701.
(10) Du, S.; Valla, J. A.; Parnas, R. S.; Bollas, G. M. Conversion of Polyethylene Terephthalate Based Waste Carpet to Benzene-Rich Oils through Thermal, Catalytic, and Catalytic Steam Pyrolysis. *ACS Sustainable Chem. Eng.* **2016**, *4*, 2852−2860.
(11) Thiounn, T.; Smith, R. C. Advances and approaches for chemical recycling of plastic waste. *J. Polym. Sci.* **2020**, *58*, 1347−1364.
(12) Garcia, J. M.; Robertson, M. L. The future of plastics recycling. *Science* **2017**, *358*, 870−872.
(13) Furukawa, M.; Kawakami, N.; Tomizawa, A.; Miyamoto, K. Efficient Degradation of Poly(ethylene terephthalate) with Thermobifida fusca Cutinase Exhibiting Improved Catalytic Activity Generated using Mutagenesis and Additive-based Approaches. *Sci. Rep.* **2019**, *9*, 16038.
(14) Chen, C.-C.; Dai, L.; Ma, L.; Guo, R.-T. Enzymatic degradation of plant biomass and synthetic polymers. *Nature Reviews Chemistry* **2020**, *4*, 114−126.
(15) Chen, S.; Su, L.; Chen, J.; Wu, J. Cutinase: characteristics, preparation, and application. *Biotechnol. Adv.* **2013**, *31*, 1754−1767.
(16) Kawai, F.; Kawabata, T.; Oda, M. Current knowledge on enzymatic PET degradation and its possible application to waste stream management and other fields. *Appl. Microbiol. Biotechnol.* **2019**, *103*, 4253−4268.
(17) Castro, A. M. d.; Carniel, A.; Stahelin, D.; Chinelatto Junior, L. S.; Honorato, H. d. A.; de Menezes, S. M. C. High-fold improvement of assorted post-consumer poly(ethylene terephthalate) (PET) packages hydrolysis using Humicola insolens cutinase as a single biocatalyst. *Process Biochem.* **2019**, *81*, 85−91.
(18) Barth, M.; Oeser, T.; Wei, R.; Then, J.; Schmidt, J.; Zimmermann, W. Effect of hydrolysis products on the enzymatic degradation of polyethylene terephthalate nanoparticles by a polyester hydrolase from Thermobifida fusca. *Biochem. Eng. J.* **2015**, *93*, 222−228.
(19) Ronkvist, Å. M.; Xie, W.; Lu, W.; Gross, R. A. Cutinase-Catalyzed Hydrolysis of Poly(ethylene terephthalate). *Macromolecules* **2009**, *42*, 5128−5138.
(20) Then, J.; Wei, R.; Oeser, T.; Barth, M.; Belisario-Ferrari, M. R.; Schmidt, J.; Zimmermann, W. Ca2+ and Mg2+ binding site engineering increases the degradation of polyethylene terephthalate films by polyester hydrolases from Thermobifida fusca. *Biotechnol. J.* **2015**, *10*, 592−598.
(21) Then, J.; Wei, R.; Oeser, T.; Gerdts, A.; Schmidt, J.; Barth, M.; Zimmermann, W. A disulfide bridge in the calcium binding site of a polyester hydrolase increases its thermal stability and activity against polyethylene terephthalate. *FEBS Open Bio* **2016**, *6*, 425−432.
(22) Sulaiman, S.; Yamato, S.; Kanaya, E.; Kim, J. J.; Koga, Y.; Takano, K.; Kanaya, S. Isolation of a novel cutinase homolog with polyethylene terephthalate-degrading activity from leaf-branch compost by using a metagenomic approach. *Appl. Environ. Microbiol.* **2012**, *78*, 1556−1562.
(23) Sulaiman, S.; You, D. J.; Kanaya, E.; Koga, Y.; Kanaya, S. Crystal structure and thermodynamic and kinetic stability of metagenome-derived LC-cutinase. *Biochemistry* **2014**, *53*, 1858−1869.
(24) Sonnendecker, C.; Oeser, J.; Richter, P. K.; Hille, P.; Zhao, Z.; Fischer, C.; Lippold, H.; Blazquez-Sanchez, P.; Engelberger, F.; Ramirez-Sarmiento, C. A.; Oeser, T.; Lihanova, Y.; Frank, R.; Jahnke, H. G.; Billig, S.; Abel, B.; Strater, N.; Matysik, J.; Zimmermann, W. Low Carbon Footprint Recycling of Post-Consumer PET Plastic with a Metagenomic Polyester Hydrolase. *ChemSusChem* **2021**, DOI: 10.1002/cssc.202101062.
(25) Zhong-Johnson, E. Z. L.; Voigt, C. A.; Sinskey, A. J. An absorbance method for analysis of enzymatic degradation kinetics of poly(ethylene terephthalate) films. *Sci. Rep.* **2021**, *11*, 928.
(26) Belisario-Ferrari, M. R.; Wei, R.; Schneider, T.; Honak, A.; Zimmermann, W. Fast Turbidimetric Assay for Analyzing the Enzymatic Hydrolysis of Polyethylene Terephthalate Model Substrates. *Biotechnol. J.* **2019**, *14*, No. 1800272.
(27) Pirillo, V.; Pollegioni, L.; Molla, G. Analytical methods for the investigation of enzyme-catalyzed degradation of polyethylene terephthalate. *FEBS J.* **2021**, *288*, 4730−4745.
(28) Miksch, L.; Gutow, L.; Saborowski, R. pH-Stat Titration: A Rapid Assay for Enzymatic Degradability of Bio-Based Polymers. *Polymers* **2021**, *13*, 860.
(29) Syedd-León, R.; Sandoval-Barrantes, M.; Trimiño-Vásquez, H.; Villegas-Peñaranda, L. R.; Rodríguez-Rodríguez, G. Revisiting the fundamentals of p-nitrophenol analysis for its application in the quantification of lipases activity. A graphical update. *Uniciencia* **2020**, *34*, 31−43.
(30) Fang, X.; Mark, G.; von Sonntag, C. OH radical formation by ultrasound in aqueous solutions Part I: the chemistry underlying the terephthalate dosimeter. *Ultrason. Sonochem.* **1996**, *3*, 57−63.
(31) Yang, X. F.; Guo, X. Q. Fe(II)-EDTA chelate-induced aromatic hydroxylation of terephthalate as a new method for the evaluation of hydroxyl radical-scavenging ability. *Analyst* **2001**, *126*, 928−932.
(32) Wei, R.; Oeser, T.; Billig, S.; Zimmermann, W. A high-throughput assay for enzymatic polyester hydrolysis activity by fluorimetric detection. *Biotechnol. J.* **2012**, *7*, 1517−1521.
(33) Erickson, E.; Shakespeare, T. J.; Bratti, F.; Buss, B. L.; Graham, R.; Hawkins, M. A.; Konig, G.; Michener, W. E.; Miscall, J.; Ramirez, K. J.; Rorrer, N. A.; Zahn, M.; Pickford, A. R.; McGeehan, J. E.; Beckham, G. T. Comparative Performance of PETase as a Function of Reaction Conditions, Substrate Properties, and Product Accumulation. *ChemSusChem* **2021**, DOI: 10.1002/cssc.202101932.
(34) Rodríguez-Hernández, A. G.; Muñoz-Tabares, J. A.; Aguilar-Guzmán, J. C.; Vazquez-Duhalt, R. A novel and simple method for polyethylene terephthalate (PET) nanoparticle production. *Environ. Sci.: Nano* **2019**, *6*, 2031−2036.
(35) Vogel, K.; Wei, R.; Pfaff, L.; Breite, D.; Al-Fathi, H.; Ortmann, C.; Estrela-Lopis, I.; Venus, T.; Schulze, A.; Harms, H.; Bornscheuer, U. T.; Maskow, T. Enzymatic degradation of polyethylene terephthalate nanoplastics analyzed in real time by isothermal titration calorimetry. *Sci. Total Environ.* **2021**, *773*, 145111.
(36) Wei, R.; Oeser, T.; Schmidt, J.; Meier, R.; Barth, M.; Then, J.; Zimmermann, W. Engineered bacterial polyester hydrolases efficiently degrade polyethylene terephthalate due to relieved product inhibition. *Biotechnol. Bioeng.* **2016**, *113*, 1658−1665.
(37) Sabot, A.; Krause, S. Simultaneous Quartz Crystal Microbalance Impedance and Electrochemical Impedance Measurements. Investigation into the Degradation of Thin Polymer Films. *Anal. Chem.* **2002**, *74*, 3304−3311.

(38) Fernández-Sánchez, C.; McNeil, C. J.; Rawson, K. Electrochemical impedance spectroscopy studies of polymer degradation: application to biosensor development. *TrAC, Trends Anal. Chem.* **2005**, *24*, 37−48.
(39) Randles, J. E. B. Kinetics of rapid electrode reactions. *Discuss. Faraday Soc.* **1947**, *1*, 11.
(40) Ahmed, R.; Reifsnider, K. Study of Influence of Electrode Geometry on ImpedanceSpectroscopy. *ASME 2010 8th International Fuel Cell Science, Engineering and TechnologyConference* **2010**, *2*, 167−175.
(41) Both, J. Electrolytic capacitors, 1890 to 1925: early history and basic principle. *IEEE Electrical Insulation Magazine* **2015**, *31*, 22−29.
(42) Küchler, F.; Färber, R.; Franck, C. M. *in 2020 IEEE Electrical Insulation Conference (EIC)* **2020**, 179−183.
(43) Zhao, Y. P.; Wang, G. C.; Lu, T. M.; Palasantzas, G.; De Hosson, J. T. M. Surface-roughness effect on capacitance and leakage current of an insulating film. *Phys. Rev. B: Condens. Matter Mater. Phys.* **1999**, *60*, 9157−9164.
(44) McLaren, J. W.; Nau, C. B.; Erie, J. C.; Bourne, W. M. Corneal thickness measurement by confocal microscopy, ultrasound, and scanning slit methods. *Am. J. Ophthalmol.* **2004**, *137*, 1011−1020.
(45) Ollis, D. L.; Cheah, E.; Cygler, M.; Dijkstra, B.; Frolow, F.; Franken, S. M.; Harel, M.; Remington, S. J.; Silman, I.; Schrag, J.; Sussman, J. L.; Verschueren, K. H. G.; Goldman, A. The α/β hydrolase fold. *Protein Eng., Des. Sel.* **1992**, *5*, 197−211.
(46) Dimitriou, P. S.; Denesyuk, A.; Takahashi, S.; Yamashita, S.; Johnson, M. S.; Nakayama, T.; Denessiouk, K. Alpha/beta-hydrolases: A unique structural motif coordinates catalytic acid residue in 40 protein fold families. *Proteins: Struct., Funct., Genet.* **2017**, *85*, 1845−1855.
(47) Goldsmith, M.; Tawfik, D. S. Enzyme engineering: reaching the maximal catalytic efficiency peak. *Curr. Opin. Struct. Biol.* **2017**, *47*, 140−150.
(48) Liu, B.; Lu, X.; Ju, Z.; Sun, P.; Xin, J.; Yao, X.; Zhou, Q.; Zhang, S. Ultrafast Homogeneous Glycolysis of Waste Polyethylene Terephthalate via a Dissolution-Degradation Strategy. *Ind. Eng. Chem. Res.* **2018**, *57*, 16239−16245.
(49) Wang, S. H.; Meng, X. H.; Zhou, H.; Liu, Y.; Secundo, F.; Liu, Y. Enzyme Stability and Activity in Non-Aqueous Reaction Systems: A Mini Review. *Catalysts* **2016**, *6*, 32.
(50) Jahnke, H. G.; Krinke, D.; Seidel, D.; Lilienthal, K.; Schmidt, S.; Azendorf, R.; Fischer, M.; Mack, T.; Striggow, F.; Althaus, H.; Schober, A.; Robitzki, A. A. A novel 384-multiwell microelectrode array for the impedimetric monitoring of Tau protein induced neurodegenerative processes. *Biosens. Bioelectron.* **2017**, *88*, 78−84.
(51) Steude, A.; Schmidt, S.; Robitzki, A. A.; Panke, O. An electrode array for electrochemical immuno-sensing using the example of impedimetric tenascin C detection. *Lab Chip* **2011**, *11*, 2884−2892.

https://doi.org/10.1021/acscatal.1c03963
ACS Catal. 2022, 12, 25−35